

A numerical model for multigroup radiation hydrodynamics

N. Vaytet, E. Audit

Service d'Astrophysique, CEA/DSM/IRFU/SAP, Centre d'Études de Saclay, L'Orme des Merisiers, 91191 Gif-sur-Yvette, Cedex, France

B. Dubroca

CELIA, Université Bordeaux I, CNRS, CEA, 33405 Talence, France

F. Delahaye

LERMA, Observatoire de Paris, ENS, UPMC, UCP, CNRS, 5 Place Jules Janssen, 92190 Meudon, France

Abstract

We present in this paper a multigroup model for radiation hydrodynamics to account for variations of the gas opacity as a function of frequency. The entropy closure model (M_1) is applied to multigroup radiation transfer in a radiation hydrodynamics code. In difference from the previous grey model, we are able to reproduce the crucial effects of frequency-variable gas opacities, a situation omnipresent in physics and astrophysics. We also account for the energy exchange between neighbouring groups which is important in flows with strong velocity divergence. These terms were computed using a finite volume method in the frequency domain. The radiative transfer aspect of the method was first tested separately for global consistency (reversion to grey model) and against a well established kinetic model through Marshak wave tests with frequency dependent opacities. Very good agreement between the multigroup M_1 and kinetic models was observed in all tests. The successful coupling of the multigroup radiative transfer to the hydrodynamics was then confirmed through a second series of tests. Finally, the model was linked to a database of opacities for a Xe gas in order to simulate realistic multigroup radiative shocks in Xe. The differences with the previous grey models are discussed.

Keywords: Radiative transfer, Moment model, Multigroup, Laboratory astrophysics
PACS: 47.70.Mc

1. Introduction

The study of radiative transfer and its interaction with matter has an extremely wide range of applications ranging from medical imagery to astrophysics. In many cases, as for example in stellar atmospheres, the radiation is considered as a physical probe which provides access to the thermodynamical properties of the flow through the spectrum of emission and absorption lines. However, the radiation often has a very important dynamical role in the system. It cannot only be considered as a passive probe, but as an integral part of the equations governing the system dynamics.

The equation of radiative transfer (ignoring scattering) is

$$\left(\frac{1}{c}\frac{\partial}{\partial t} + \mathbf{n} \cdot \nabla\right) I(\mathbf{x}, t; \mathbf{n}, \nu) = \sigma_\nu \left(B(\mathbf{x}, t, \nu) - I(\mathbf{x}, t; \mathbf{n}, \nu)\right) \quad (1)$$

where I is the specific intensity of the radiation, ν the frequency, c is the speed of light, σ_ν the absorption/emission coefficient and B the black body specific intensity. \mathbf{n} , \mathbf{x} , and t are the angular, spatial and temporal variables, respectively. As the radiation intensity depends on seven variables in three-dimensions, solving the full transfer equation coupled to the hydrodynamics to tackle radiation hydrodynamics (RHD) problems is still out of reach of modern computational architectures, even with the remarkable and constant increase in computing power.

In order to overcome this difficulty, much effort has been spent in recent years developing mathematically less complicated, yet accurate approximations to the equations of radiative transfer. Such approximations include diffusion approximations [8, 10, 9] and moment models [5, 11, 17, 21]. All of these approximations use frequency and/or angle-integrated variables which greatly simplify the calculations. The approximations due to the angular integration have been widely studied (see for example Olson et al. [18]). However, in many situations, the quantities involved in the equations of radiative transfer (in particular the absorption and scattering coefficients) depend strongly on frequency, and the so called ‘grey’ approximation (integrated over all frequencies) is no longer appropriate. Only very recently

have models which take into account variations in frequency been developed [22, 19, 1, 20]. The common practise is to split the frequency domain into a finite number of bins or groups and the equations of radiative transfer are solved within each group; this is known as a multigroup method. Such a scheme is then capable of allowing for gas opacity variations in the frequency domain providing a more accurate description of radiative transfer processes. The model we present in this paper is an extension of the moment model introduced in Turpault [22] which couples the frequency-dependent radiation to the hydrodynamics.

Moment models are obtained by computing successive angular moments of the radiative transfer equation. One obtains a hierarchy of equations for moments of the specific intensity. Basically, each equation describes the evolution of the n^{th} moment as a function of the divergence of the $(n+1)^{\text{th}}$ moment. For instance, the equations giving the evolution of the first two moments are

$$\begin{aligned} \partial_t E_\nu + \nabla \cdot \mathbf{F}_\nu &= \sigma_\nu(4\pi B - cE_\nu) \\ \partial_t \mathbf{F}_\nu + c^2 \nabla \cdot \mathbb{P}_\nu &= -\sigma_\nu c \mathbf{F}_\nu \end{aligned} \quad (2)$$

where E_ν , \mathbf{F}_ν , and \mathbb{P}_ν are, respectively, the radiative energy density, the radiative energy flux, and the radiative pressure, which are defined in terms of the zeroth, first and second moments of the specific intensity as

$$\begin{aligned} E_\nu &= \frac{1}{c} \oint I(\mathbf{x}, t; \mathbf{n}, \nu) d\Omega \\ \mathbf{F}_\nu &= \oint \mathbf{n} I(\mathbf{x}, t; \mathbf{n}, \nu) d\Omega \\ \mathbb{P}_\nu &= \frac{1}{c} \oint \mathbf{n} \otimes \mathbf{n} I(\mathbf{x}, t; \mathbf{n}, \nu) d\Omega \quad . \end{aligned} \quad (3)$$

The transfer equation is formally equivalent to an infinite hierarchy of moment equations. In order to have a tractable moment model, one must cut this hierarchy at some given order. A closure relation is then needed in order to express the moment of highest order as a function of the others.

In this paper, we develop for the first time the coupling of the M_1 moment model for radiative transfer to the hydrodynamics to create a multigroup model for RHD. A finite volume method used to compute the additional terms due to frequency variations is described. We then present a series of tests for the multigroup model studying first the radiative transfer alone and then the radiation coupled to the hydrodynamics. The strengths and future developments of the model are finally discussed.

2. The multigroup model for radiation hydrodynamics

2.1. The monochromatic equations of radiation hydrodynamics

The equations of radiation hydrodynamics describe the effects of radiative transfer on a moving fluid. The fluid evolution is determined by the classical conservation equations (mass, momentum, and energy) which are coupled to the radiative transfer equations (2) through source terms characterizing the momentum and energy exchanges between the fluid and the radiation.

In order to write the RHD equations, one has to choose the frame in which to evaluate the radiative quantities: laboratory frame or comoving frame (i.e. the frame moving with the fluid). The laboratory frame is convenient because the the left-hand side of the system remains hyperbolic and thus globally conservative [14]. However in this frame, interactions with matter become complex because of Doppler and aberration effects that have to be incorporated in the source terms. On the other hand, using the radiative quantities expressed in the comoving frame [13] adds non-conservative terms to the equations, and conversions of the radiative quantities between comoving and lab frames are required in order to be compared to observations as any measurement will almost certainly be carried out in the lab frame. However the source terms coupling matter and radiation remain unaffected by the fluid motions.

We have chosen to express radiative quantities in the comoving frame for the greater simplicity of the source terms. The equations of non-relativistic RHD (to order u/c) can then be written as [13, 15, 2]

$$\begin{aligned}
 \partial_t \rho &+ \nabla \cdot (\rho \mathbf{u}) &= 0 \\
 \partial_t (\rho \mathbf{u}) &+ \nabla \cdot (\rho \mathbf{u} \otimes \mathbf{u} + p \mathbb{I}) &= \int_0^\infty (\sigma_\nu/c) \mathbf{F}_\nu d\nu \\
 \partial_t e &+ \nabla \cdot (\mathbf{u}(e + p)) &= - \int_0^\infty \left(\sigma_\nu (4\pi B - cE_\nu) \right. \\
 &&\quad \left. - (\sigma_\nu/c) \mathbf{u} \cdot \mathbf{F}_\nu \right) d\nu
 \end{aligned} \tag{4}$$

$$\begin{aligned}
 \partial_t E_\nu + \nabla \cdot \mathbf{F}_\nu + \mathbb{P}_\nu : \nabla \mathbf{u} + \nabla \cdot (\mathbf{u} E_\nu) - \partial_\nu (\nu \mathbb{P}_\nu) : \nabla \mathbf{u} &= \sigma_\nu (4\pi B - cE_\nu) \\
 \partial_t \mathbf{F}_\nu + c^2 \nabla \cdot \mathbb{P}_\nu + \mathbf{F}_\nu \cdot \nabla \mathbf{u} + \nabla \cdot (\mathbf{u} \otimes \mathbf{F}_\nu) - \partial_\nu (\nu \mathbb{Q}_\nu) : \nabla \mathbf{u} &= -\sigma_\nu c \mathbf{F}_\nu
 \end{aligned} \tag{5}$$

where ρ is the gas density, u the velocity, e the total gas energy, p the gas pressure, and \mathbb{Q}_ν is the third moment of the specific intensity

$$\mathbb{Q}_\nu = \oint \mathbf{n} \otimes \mathbf{n} \otimes \mathbf{n} I(\mathbf{x}, t; \mathbf{n}, \nu) d\Omega \quad . \tag{6}$$

The tensorial contractions are defined by $\mathbb{P} : \nabla \mathbf{u} = \mathbb{P}_{ij} \partial^i u^j$ and $\mathbb{Q} : \nabla \mathbf{u} = \mathbb{Q}_{ijk} \partial^i u^j$.

2.2. The multigroup equations of radiation hydrodynamics

Equations (4) and (5) are all Eulerian, but the radiative quantities are evaluated in the frame comoving with the fluid. In a grey model, system (5) is integrated from 0 to ∞ in frequency and the terms involving frequency derivatives $\partial_\nu(\nu \mathbb{P}_\nu)$ and $\partial_\nu(\nu \mathbb{Q}_\nu)$ vanish. However, in a multigroup model these terms remain and are in fact of great importance; they govern energy transfers between neighbouring groups.

In a multigroup model, the frequency domain is divided into a finite number of bins or groups and the radiative transfer equations are integrated and solved within each group. The integrals in the source terms of the hydrodynamic equations (4) then become sums of source terms over the total number of groups. Systems (4) and (5) become

$$\begin{aligned}
\partial_t \rho &+ \nabla \cdot (\rho \mathbf{u}) &= 0 \\
\partial_t (\rho \mathbf{u}) &+ \nabla \cdot (\rho \mathbf{u} \otimes \mathbf{u} + p \mathbb{I}) &= \sum_{g=1}^{N_g} (\sigma_{Fg}/c) \mathbf{F}_g \\
\partial_t e &+ \nabla \cdot (\mathbf{u}(e + p)) &= - \sum_{g=1}^{N_g} \left(c(\sigma_{Pg} \Theta_g(T) - \sigma_{Eg} E_g) \right. \\
&&&\quad \left. - (\sigma_{Fg}/c) \mathbf{u} \cdot \mathbf{F}_g \right)
\end{aligned} \tag{7}$$

$$\begin{aligned}
\partial_t E_g + \nabla \cdot \mathbf{F}_g + \nabla \cdot (\mathbf{u} E_g) + \mathbb{P}_g : \nabla \mathbf{u} - \nabla \mathbf{u} : \int_{\nu_{g-1/2}}^{\nu_{g+1/2}} \partial_\nu (\nu \mathbb{P}_\nu) d\nu \\
= c(\sigma_{Pg} \Theta_g(T) - \sigma_{Eg} E_g)
\end{aligned}$$

$$\begin{aligned}
\partial_t \mathbf{F}_g + c^2 \nabla \cdot \mathbb{P}_g + \nabla \cdot (\mathbf{u} \otimes \mathbf{F}_g) + \mathbf{F}_g \cdot \nabla \mathbf{u} - \nabla \mathbf{u} : \int_{\nu_{g-1/2}}^{\nu_{g+1/2}} \partial_\nu (\nu \mathbb{Q}_\nu) d\nu \\
= -\sigma_{Fg} c \mathbf{F}_g
\end{aligned} \tag{8}$$

with

$$X_g = \int_{\nu_{g-1/2}}^{\nu_{g+1/2}} X_\nu d\nu \tag{9}$$

where $X = E, \mathbf{F}, \mathbb{P}, \mathbb{Q}$ which represent the radiative energy, flux, pressure and heat flux inside each group g which holds frequencies between $\nu_{g-1/2}$ and $\nu_{g+1/2}$. N_g is the total number of groups and $\Theta_g(T)$ is the energy of the photons having a Planck distribution at temperature T inside a given group. The absorption coefficients σ_{Pg} , σ_{Eg} and σ_{Fg} are the means of σ_ν inside a given group weighted by the Planck function, the radiative energy and the radiative flux respectively.

In order to integrate the previous system, it is necessary to introduce a closure relation giving \mathbb{P} and \mathbb{Q} as a function of E and \mathbf{F} . The closure we have chosen is based on the M_1 model and is presented below.

2.3. The multigroup M_1 model

The M_1 model [5] uses the first two moment equations (2) to approximate the equation of radiative transfer. It has the great advantage over flux-limited diffusion models [16, 12, 11] of being valid in both the diffusion and free-streaming limits while maintaining a directionality in the propagation of the radiation. Shadows can be created with the M_1 method while flux-limited diffusion considers the radiative flux to always be colinear to the radiative temperature gradient, which can result in radiation propagating around corners [5, 7].

In the M_1 model the radiative pressure is expressed as $\mathbb{P} = \mathbb{D}E$ where \mathbb{D} is known as the Eddington tensor. The expression for \mathbb{D} is obtained by minimizing the radiative entropy which yields

$$\mathbb{D} = \frac{1 - \chi}{2} \mathbb{I} + \frac{3\chi - 1}{2} \frac{\mathbf{F} \otimes \mathbf{F}}{\|\mathbf{F}\|^2} \quad (10)$$

where

$$\chi = \frac{3 + 4f^2}{5 + 2\sqrt{4 - 3f^2}} \quad (11)$$

and $f = \frac{\|\mathbf{F}\|}{cE}$ is the ratio of the grey flux to the flux free-streaming limit, also known as the reduced flux. The quantities without the subscript ν represent quantities integrated over the entire frequency range. Note that by definition of E and \mathbf{F} , we have $f \leq 1$, which implies that the radiative energy is transported at most at the speed of light. In one dimension we simply have $\mathbb{P} = \chi E$. We have plotted χ in Fig. 1 as a function of f (red). This closure relation recovers the two asymptotic regimes of radiative transfer. In the free-streaming limit (i.e. transparent media), we have $f = 1$ and $\chi = 1$. On

the other hand, in the diffusion limit, $f = 0$ and $\chi = 1/3$, which corresponds to an isotropic radiation pressure.

In order to express the radiative heat flux \mathbb{Q} as a function of the lower angular moments using the M_1 closure, we define $\mathbb{Q} = \mathbb{H}Ec$. Due to the symmetry of the specific intensity distribution function around the axis defined by the direction of propagation of the radiative flux, it can be shown that

$$\mathbb{H} = \varphi_1(\mathbf{f}_i\delta_{jk} + \mathbf{f}_j\delta_{ik} + \mathbf{f}_k\delta_{ij}) + \varphi_2(\mathbf{f}_i\mathbf{f}_j\mathbf{f}_k) \quad (12)$$

in which \mathbf{f}_i are the components of the reduced flux vector $\mathbf{f} = \frac{\mathbf{F}}{cE}$,

$$\varphi_1 = \frac{(f-2+a)(f+2-a)}{4f(a-2)^5} \left[12 \ln \left(\frac{f-2+a}{f+2-a} \right) (f^4 + 2af^2 - 7f^2 - 4a + 8) \right. \\ \left. + 48f^3 - 9af^3 - 80f + 40af \right] \quad (13)$$

and

$$\varphi_2 = \frac{1}{f^3(a-2)^5} \left[60 \ln \left(\frac{f-2+a}{f+2-a} \right) (-f^6 + 15f^4 - 3af^4 + 15af^2 - 42f^2 \right. \\ \left. - 16a + 32) + 54af^5 - 465f^5 - 674af^3 + 2140f^3 + 1056af - 2112f \right] \quad (14)$$

where $a = \sqrt{4 - 3f^2}$. We plot φ_1 and φ_2 as a function of f in Fig. 1 (green and blue). Note that in one dimension, $\mathbf{f} = (f, 0, 0)$ and we have $\mathbb{Q} = \psi Ec$ where

$$\psi = 3\varphi_1 f + \varphi_2 f^3 \quad (15)$$

and ψ is plotted in Fig. 1 (orange). This fully defines the evolution of the radiative energy and pressure of the model coupled to the hydrodynamics of the system.

A natural way to extend this closure to a multigroup model would be to minimize the total radiative entropy, which is a rather complex procedure. However, Turpault [22] has shown that applying inside each group a closure formally equivalent to the M_1 closure leads to almost indistinguishable results; a strategy which we have therefore adopted for its greater simplicity. We define for each group the radiative pressure as $\mathbb{P}_g = \mathbb{D}_g E_g$ where

$$\mathbb{D}_g = \frac{1 - \chi_g}{2} \mathbb{I} + \frac{3\chi_g - 1}{2} \frac{\mathbf{F}_g \otimes \mathbf{F}_g}{\|\mathbf{F}_g\|^2}, \quad (16)$$

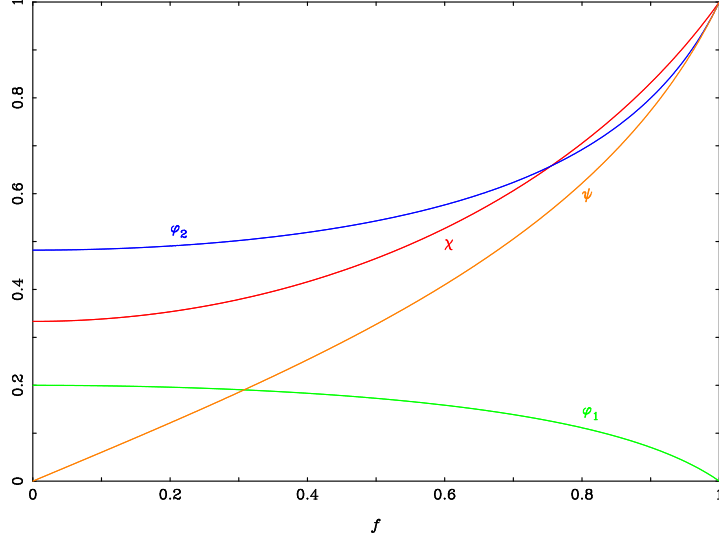


Figure 1: χ (red), φ_1 (green), φ_2 (blue) and ψ (orange) as a function of f . χ , φ_1 and φ_2 are symmetric with respect to the ordinates axis, ψ is symmetric with respect to the origin.

$$\chi_g = \frac{3 + 4f_g^2}{5 + 2\sqrt{4 - 3f_g^2}} \quad (17)$$

and $f_g = \frac{\|\mathbf{F}_g\|}{cE_g}$. The heat flux $Q_g = \mathbb{H}_g E_g c$ is computed in the same manner.

2.4. A finite volume method for the frequency derivatives

The only terms which were not included in our previous grey RHD models [7] are the terms in (8) involving the frequency differentials. In order to evaluate these terms, we adopt a finite volume method in the frequency dimension. We present here this method in the one-dimensional case, but its extension to several dimensions is trivial. Retaining only the time and frequency derivatives of the radiative energy and flux equations of system (5), we obtain

$$\begin{aligned} \partial_t E_\nu - \mathcal{D} \partial_\nu (\nu \mathbb{P}_\nu) &= 0 \\ \partial_t \mathbf{F}_\nu - \mathcal{D} \partial_\nu (\nu \mathbb{Q}_\nu) &= 0 \end{aligned} \quad (18)$$

where $\mathcal{D} = \nabla \cdot \mathbf{u}$. We now assume that the frequency group boundaries ($\nu_{g\pm 1/2}$) are equivalent to the volume elements' boundaries in the frequency

dimension. The finite volume discretization of (18) gives

$$\begin{aligned} \frac{E_g^{n+1} - E_g^n}{\Delta t} - \mathcal{D} \left(\nu_{g+1/2} \mathbb{P}_{g+1/2}^n - \nu_{g-1/2} \mathbb{P}_{g-1/2}^n \right) &= 0 \\ \frac{\mathbf{F}_g^{n+1} - \mathbf{F}_g^n}{\Delta t} - \mathcal{D} \left(\nu_{g+1/2} \mathbb{Q}_{g+1/2}^n - \nu_{g-1/2} \mathbb{Q}_{g-1/2}^n \right) &= 0 \end{aligned} \quad (19)$$

where $\mathbb{P}_{g\pm 1/2}$ and $\mathbb{Q}_{g\pm 1/2}$ are the radiative pressures and heat flux evaluated at the group interfaces. The Jacobian matrix \mathcal{J} of the hyperbolic system (18) is given by

$$\mathcal{J} = -\mathcal{D}\nu \tilde{\mathcal{J}} \quad \text{with} \quad \tilde{\mathcal{J}} = \frac{\partial \begin{pmatrix} \mathbb{P}_\nu \\ \mathbb{Q}_\nu \end{pmatrix}}{\partial \begin{pmatrix} E_\nu \\ \mathbf{F}_\nu \end{pmatrix}} = \begin{pmatrix} \chi - f\chi' & \chi' \\ c\psi - cf\psi' & \psi' \end{pmatrix} \quad (20)$$

where $'$ denotes derivatives with respect to f . It can be shown that the trace and the determinant of $\tilde{\mathcal{J}}$ are both strictly positive. The eigenvalues of system (18) are thus always of the same sign (i.e. opposite to that of \mathcal{D}), which enables us to use a standard upwind scheme with respect to \mathcal{D} to calculate the values for \mathbb{P} and \mathbb{Q} at the group interfaces. This yields

$$\begin{aligned} \mathbb{X}_{g-1/2} &= \begin{cases} \mathbb{X}_g / \Delta\nu_g & \text{if } \mathcal{D} > 0 \\ \mathbb{X}_{g-1} / \Delta\nu_{g-1} & \text{if } \mathcal{D} \leq 0 \end{cases} \\ \mathbb{X}_{g+1/2} &= \begin{cases} \mathbb{X}_{g+1} / \Delta\nu_{g+1} & \text{if } \mathcal{D} > 0 \\ \mathbb{X}_g / \Delta\nu_g & \text{if } \mathcal{D} \leq 0 \end{cases} \end{aligned} \quad (21)$$

where $\mathbb{X} = \mathbb{P}$ or \mathbb{Q} . This shows that the radiative energy and flux are advected from one group to the other depending on the sign of the velocity divergence. It is straightforward to show that the inclusion of these terms preserves the flux limitation condition $|f| \leq 1$ as long as $\psi < \chi$, which is always true (see Fig. 1). It would of course be possible to use higher order schemes to evaluate the quantities at the group interfaces by computing slopes using the usual methods. For the sake of conciseness this will not be explicated here.

3. Numerical method and tests

3.1. Numerical method

In this section, we briefly present our global strategy to integrate the coupled RHD system (7)-(8) (the method is identical to the one reported in

González et al. [7] apart from the terms involving the frequency differentials which were not included). In order to have a tractable time step, the radiative transport needs to be treated implicitly. However, it is most of the time more efficient to retain an explicit scheme for the hydrodynamics. We therefore use the following splitting scheme.

In the first step the hydrodynamics system (7) is solved explicitly without the source terms. It is integrated using a classical second order MUSCL-Hancock scheme. In the second step, the radiation and the coupling terms are solved implicitly. The terms in system (8) involving frequency derivatives are discretized as presented above and using the velocity divergence from the hydrodynamic solver. The velocity coming from the hydrodynamic solver is also used to discretize the other terms involving velocity derivatives. For the hyperbolic radiative term (two first left hand-side terms of system (8)) we use a HLLC solver with an asymptotic preserving correction in order to recover properly the diffusion limit [3]. System (8) is solved implicitly with the source terms of system (7) using a Raphson-Newton procedure.

$$\text{Step 1} \begin{cases} \partial_t \rho & + \nabla \cdot (\rho \mathbf{u})^n & = 0 \\ \partial_t (\rho \mathbf{u}) & + \nabla \cdot (\rho \mathbf{u} \otimes \mathbf{u} + p \mathbb{I})^n & = 0 \\ \partial_t e & + \nabla \cdot (\mathbf{u}(e + p))^n & = 0 \end{cases} \quad (22)$$

$$\text{Step 2} \begin{cases} \partial_t E_g + \nabla \cdot \mathbf{F}_g^{n+1} + \nabla \cdot (\mathbf{u} E_g)^{n+1} + (\mathbb{P}_g : \nabla \mathbf{u})^{n+1} \\ \quad - (\nabla \mathbf{u} : \tilde{\mathbb{P}}_g)^{n+1} = c(\sigma_{Pg} \Theta_g(T) - \sigma_{Eg} E_g)^{n+1} \\ \partial_t \mathbf{F}_g + c^2 \nabla \cdot \mathbb{P}_g^{n+1} + \nabla \cdot (\mathbf{u} \otimes \mathbf{F}_g)^{n+1} + (\mathbf{F}_g \cdot \nabla \mathbf{u})^{n+1} \\ \quad - (\nabla \mathbf{u} : \tilde{\mathbb{Q}}_g)^{n+1} = -(\sigma_{Fg} c \mathbf{F}_g)^{n+1} \\ \partial_t e = - \sum_{g=1}^{Ng} \left(c(\sigma_{Pg} \Theta_g(T) - \sigma_{Eg} E_g) - (\sigma_{Fg}/c) \mathbf{u} \cdot \mathbf{F}_g \right)^{n+1} \\ \partial_t (\rho u) = \sum_{g=1}^{Ng} \left((\sigma_{Fg}/c) \mathbf{F}_g \right)^{n+1} \end{cases} \quad (23)$$

where

$$\tilde{\mathbb{P}}_g = \int_{\nu_{g-1/2}}^{\nu_{g+1/2}} \partial_\nu (\nu \mathbb{P}_\nu) d\nu \quad \text{and} \quad \tilde{\mathbb{Q}}_g = \int_{\nu_{g-1/2}}^{\nu_{g+1/2}} \partial_\nu (\nu \mathbb{Q}_\nu) d\nu \quad . \quad (24)$$

The discretization of the divergence of a quantity \mathcal{U} in cell i is done

following

$$\nabla \cdot \mathcal{U} = \frac{\mathcal{U}_{i+\frac{1}{2}}^* - \mathcal{U}_{i-\frac{1}{2}}^*}{\Delta x} \quad (25)$$

where the state $\mathcal{U}_{i+\frac{1}{2}}^*$ is the value of the quantity \mathcal{U} (hydrodynamic or radiative) at the interface $i + \frac{1}{2}$ (between cell i and $i + 1$) solution to the Riemann problem with left and right states $\mathcal{U}_{i+\frac{1}{2}}^-$ and $\mathcal{U}_{i+\frac{1}{2}}^+$, respectively. For a first order scheme $\mathcal{U}_{i+\frac{1}{2}}^- = \mathcal{U}_i$ and $\mathcal{U}_{i+\frac{1}{2}}^+ = \mathcal{U}_{i+1}$. For a second order scheme, the values of \mathcal{U} are linearly extrapolated to the interfaces using local gradients.

It is of course possible to solve systems (7)-(8) without splitting using a fully implicit scheme. We have tried this in one dimension and did not find any significant differences with the splitting scheme presented above.

Calculating φ_1 and φ_2 for every grid cell at every timestep is computationally demanding due to the presence of logarithm and power functions, and we have thus tabulated the functions using 100 points which are read in once by the code at the beginning of a run. A specific value of φ_1 or φ_2 is then found using a Hermitian cubic spline interpolation which is very fast and accurate; the errors between the interpolated and the true values are less than 0.01% throughout.

In this section we validate the method for multigroup RHD using a series of tests. For this purpose the numerical scheme sketched above have been implemented in a one-dimensional Lagrangian hydrodynamic code.

The boundary conditions are implemented using two ghost cells at the edges of the grid. These ghost cells are filled using various physical constraints such as null gradient, reflexive boundary or user imposed conditions.

We use a step by step progression in our test sequence in order to verify each aspect of the method with increasingly complex problems. We first make sure that the multigroup transfer model (no hydrodynamics included) is equivalent to a grey model if the opacities are independent of frequency. We then test the multigroup aspect of the method with frequency dependent opacities. We compare the results of these tests to a well-established kinetic model which solves the equation of radiative transfer (1) directly [4]. Thirdly, we investigate the coupling of the radiative transfer to the gas motion using ‘frozen hydrodynamics’. Finally, we perform full RHD tests.

3.2. Marshak waves

3.2.1. Classical grey Marshak wave

Our first test is to check that the multigroup model reduces to a grey M_1 model for a gas with a frequency-independent opacity. We run a Marshak wave simulation, where the gas inside the grid is at rest with a uniform density $\rho = 10^{-3} \text{ g cm}^{-3}$, temperature $T = 300 \text{ K}$ in equilibrium with the radiation and opacity $\kappa = 1000 \text{ cm}^2 \text{ g}^{-1}$ independent of frequency, noting that $\sigma = \kappa\rho$. The specific heat capacity of the gas is set so that $\rho C_V = 10^{-3} \text{ erg g cm}^{-3} \text{ K}^{-1}$. The planar grid extends from 0 to 20 cm, using 500 cells. Boundary conditions: the radiative energy inside the left and right ghost cells is that of a black body at 1000 K and 300 K, respectively. The radiative flux inside the left and right ghost cells is zero. We ran two simulations; the first using a single frequency group from 0 to ∞ (grey model) and the second using five frequency groups evenly spaced between $\nu = 0 - 1.5 \times 10^{14} \text{ s}^{-1}$ plus a sixth group to cover the range $1.5 \times 10^{14} \text{ s}^{-1}$ to ∞ . The results are shown in Fig. 2 (solid lines), compared to the kinetic model (dashed lines), at a time $t = 1.36 \times 10^{-7} \text{ s}$.

The radiative temperature inside a particular group is defined by

$$T_r^g = \left(\frac{E_g}{a_R} \right)^{1/4} \quad (26)$$

and the total radiative temperature is

$$T_r = \left(\sum_{g=1}^{N_g} E_g / a_R \right)^{1/4} . \quad (27)$$

In the top panel, the curves from the multigroup simulation (and the kinetic model) are plotted. The curves representing the gas and radiative temperatures for the mono- and multigroup simulations were virtually indistinguishable and we show the percentage difference between them in the bottom panel. Note that the differences remain below 0.5% throughout. This shows that the multigroup scheme consistently reduces to a grey model for frequency independent opacities.

The kinetic model solves the equation of transfer directly using in this case 100 spatial zones, 64 directions and 64 frequency bins (all the results from the kinetic model have been tested for resolution convergence). For a moment model, the total radiative temperature (summed over all groups;

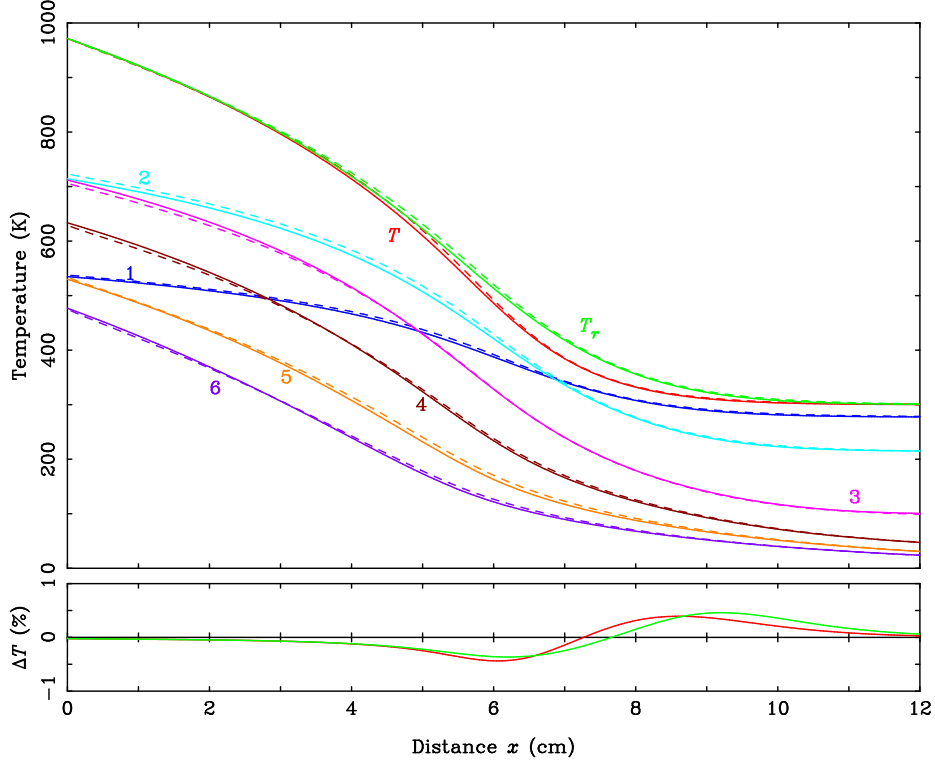


Figure 2: Top panel: Gas and radiative temperatures in the grey Marshak wave test for $\kappa(\nu) = 1000 \text{ cm}^2 \text{ g}^{-1}$ at time $t = 1.36 \times 10^{-7} \text{ s}$. The solid curves are from the multigroup M_1 model and the dashed curves represent the kinetic model. The red curve marked T is the gas temperature and the green curve marked T_r is the total radiative temperature (summed over all groups). The other coloured curves marked 1 to 6 represent the radiative temperatures inside each group. Bottom panel: percentage difference between the M_1 grey and multigroup models for the gas temperature (red) and the radiative temperature (green).

bright green) and the gas temperature (red) are in excellent agreement with their kinetic counterparts, illustrating the validity of the M_1 model for radiative transfer and proving that the multigroup model consistently reverts to a grey model in the case of frequency-independent opacities.

3.2.2. Multigroup Marshak wave with frequency dependent opacities

As a second step, we consider a frequency variable opacity in order to assess its effect on the Marshak wave test. The setup is identical to the grey test above, but the opacities in the groups 1 to 6 are (in $\text{cm}^2 \text{ g}^{-1}$) 1000, 750,

500, 250, 10 and 10 respectively. We also used 50 extra cells with steadily increasing widths at the right end of the grid in order to ensure that the radiation in the low-opacity groups does not have time to reach the right edge of the grid. The first 500 zones are the same as above, but the total grid size is ~ 9 m. The results are shown in Fig. 3 (solid lines). The gas

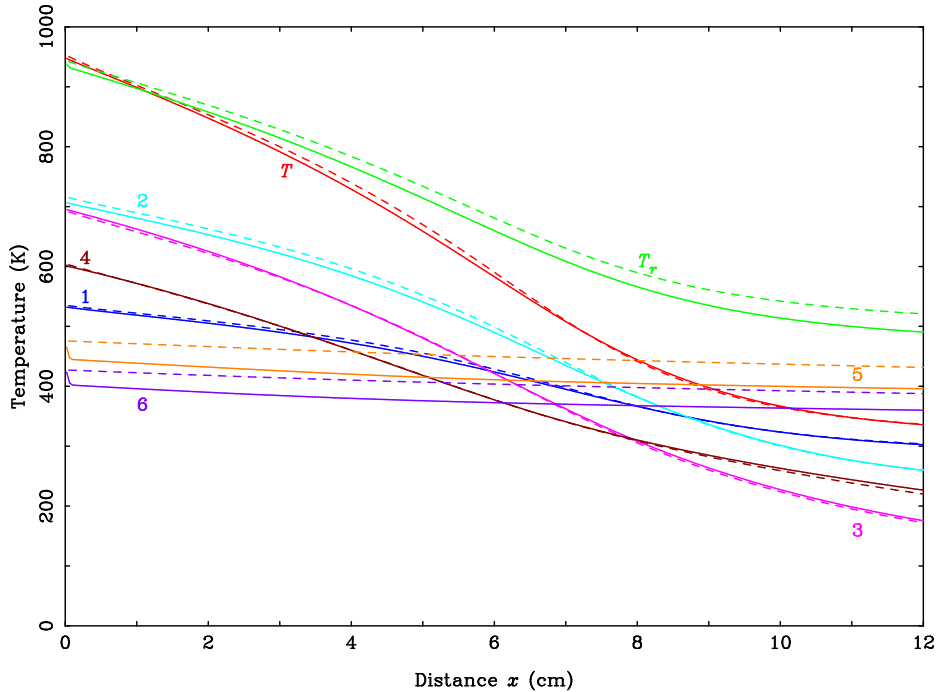


Figure 3: Same as in Fig. 2 but in the case of a frequency dependent opacity.

and radiation temperatures T and T_r are different from the ones in the first test. The radiation in the groups with weak opacities (notably groups 5 and 6) has crossed the entire grid and has heated the gas at the right edge (the gas temperature at that point is now 330 K). The radiation in the groups 3 and 4 has also travelled further than in the previous test but not as far as groups 5 and 6. We note that the radiative temperature of group 1 at the right edge is slightly higher than in the previous test (just above 300 K as opposed to 275 K). Since its opacity is unchanged, this shows that the gas has been heated by the radiation in the other groups and has re-radiated some of its energy into group 1. The curves from the kinetic model (using 400 cells, 100 directions and 512 frequencies) are also plotted (dashed lines). There is an extremely good agreement between the multigroup and kinetic

gas temperatures. The total radiative temperatures differ somewhat more than in the previous test and this difference is due to larger discrepancies in the low opacity groups 5 and 6. T_r^5 and T_r^6 are very close to their kinetic counterparts at the left edge of the grid but then drop rapidly and stabilize to a lower value. This is a boundary condition effect explained by the fact that when differences between the left and right fluxes are large (which is the case at the domain boundaries since the flux in the ghost cells is set to zero) the M_1 model becomes less accurate. A solution to this issue would be to consider an additional third moment equation or to solve two half equations (one for the flux travelling towards the left and the other towards the right) for the radiative flux [6].

3.2.3. Multigroup Marshak wave with frequency and temperature dependent opacities

In our third test we use frequency variable opacities which also vary with temperature. The setup is identical to the multigroup test above, but the opacities are set to

$$\kappa_g = \kappa_{0g} \left(\frac{T}{T_0} \right)^{3/2} \quad (28)$$

where $T_0 = 300$ K and κ_{0g} in the groups 1 to 6 are the same as in the previous test, namely (in $\text{cm}^2 \text{g}^{-1}$) 1000, 750, 500, 250, 10 and 10, respectively. The grid setup is identical to the previous test. The results are shown in Fig. 4. This time, as the gas temperature T increases, the opacity also increases and the radiation is absorbed much more rapidly, the effect being the most noticeable for groups 1 to 4 where opacities are high. We see once again an excellent agreement between the multigroup M_1 model and the kinetic model which used 512 frequencies, especially for the gas temperature.

3.3. Radiation traversing a region with strong velocity variations

The aim of this next test is to study energy exchange between groups due to Doppler effects when strong velocity variations are present in the fluid. We perform this test in vacuum ($\rho = \kappa = 0$). Radiation is cast from the left side into the computation volume, with a black-body spectrum at $T_r = 1000$ K and a unit reduced flux. The size of the box is $L = 10$ cm for 50 cells.

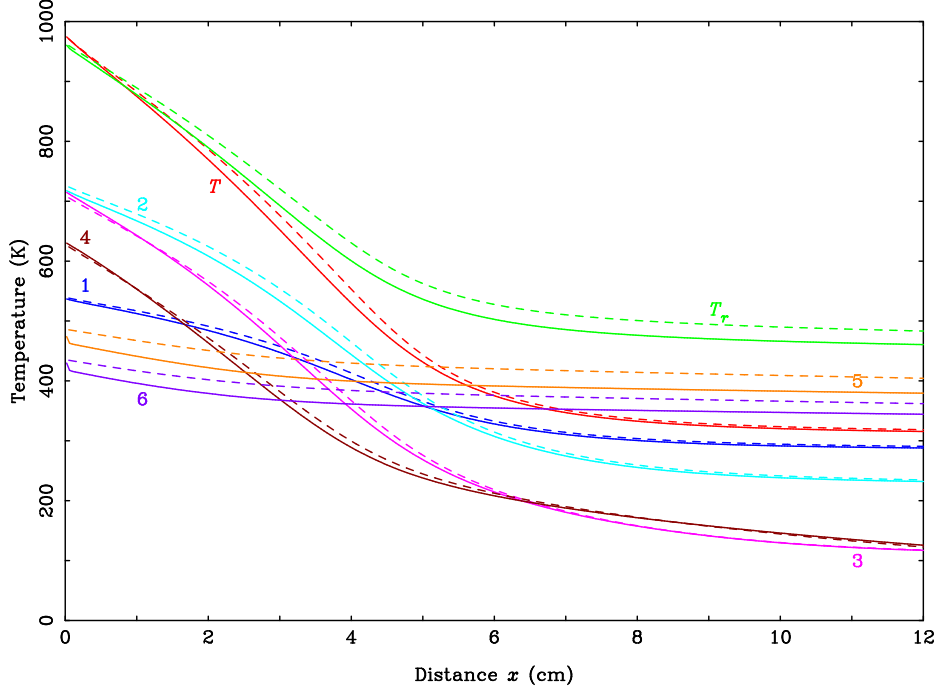


Figure 4: Same as in Fig. 3 but in the case of $\kappa(\nu) = \kappa_0(\nu)(T/T_0)^{3/2}$.

The velocity is set to obey the following law

$$u(x) = \begin{cases} 0 & \text{if } x < x_0 \\ A \sin^2\left(\frac{2\pi}{l}(x - x_0)\right) & \text{if } x_0 \leq x < x_1 \\ A & \text{if } x_1 \leq x < x_2 \\ A \sin^2\left(\frac{2\pi}{l}(x - x_0)\right) & \text{if } x_2 \leq x < x_3 \\ 0 & \text{if } x > x_3 \end{cases} \quad (29)$$

where $A = 5 \times 10^7 \text{ cm s}^{-1}$, $l = 6 \text{ cm}$, $x_0 = 2 \text{ cm}$, $x_1 = 3.5 \text{ cm}$, $x_2 = 6.5 \text{ cm}$, $x_3 = 8 \text{ cm}$ (see Fig. 5). We used 20 equally spaced frequency groups in the range $0 \rightarrow 2 \times 10^{14} \text{ Hz}$, plus a last group to hold frequencies in the range $2 \times 10^{14} \rightarrow \infty$. The radiative temperature at the boundaries is kept constant at 1000 K, and the radiative reduced flux is maintained at $f = 1$. The system is left to evolve until stationarity is reached.

The difference in radiative energies E_ν between the fixed ($u = 0$) and the moving ($u = A$) regions is shown in Fig. 6. The circles are the group

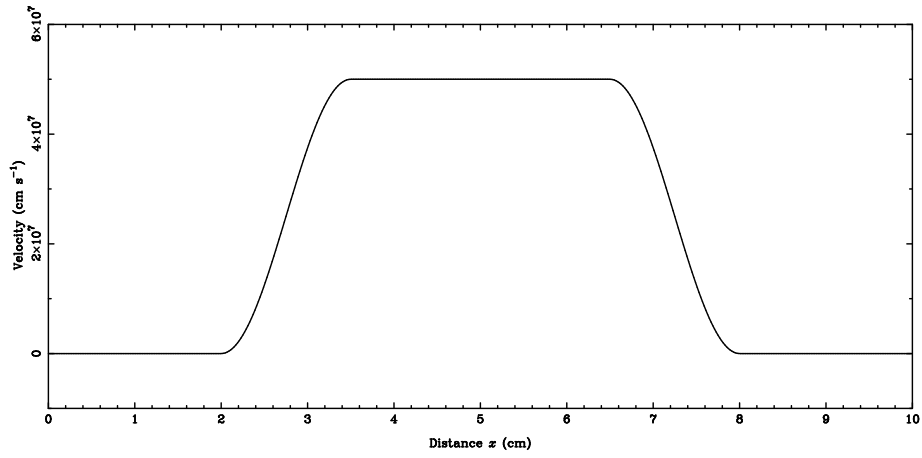


Figure 5: Gas velocity as a function of x .

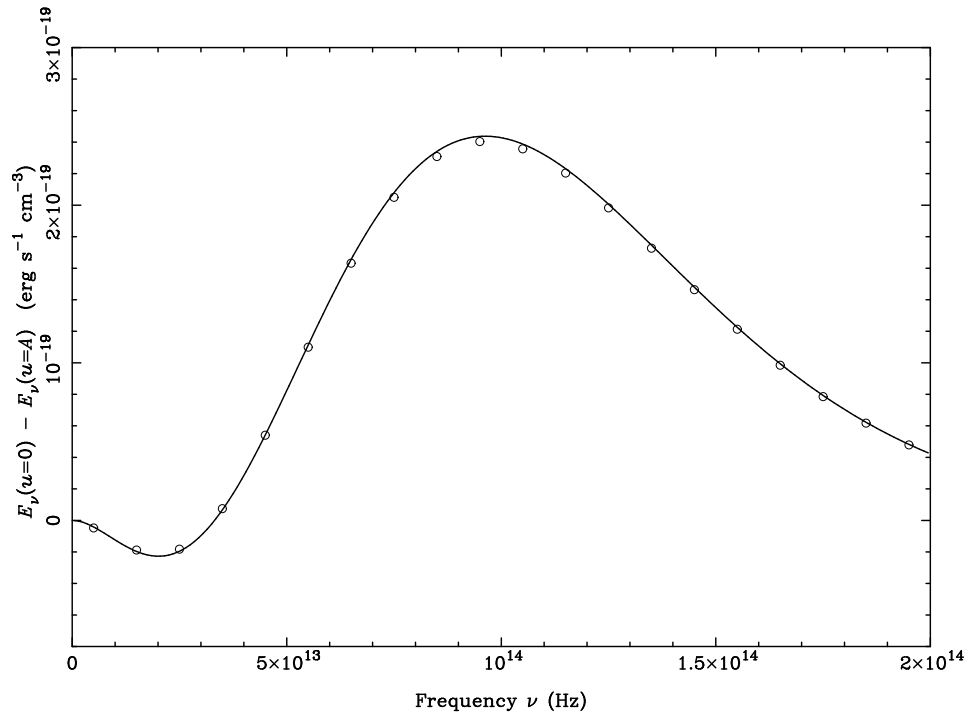


Figure 6: Difference in radiative energies between a stationary ($u = 0$) and a moving ($u = A$) black body as a function of frequency. The solid line is the analytical solution, the circles are the numerical solution.

average numerical solution. The solid line is the analytical solution, which is obtained by applying a Doppler shift in frequency to the spectrum

$$\nu' = \gamma\nu \left(1 - \frac{u}{c}\right) \quad (30)$$

where

$$\gamma = \frac{1}{\sqrt{1 - \left(\frac{u}{c}\right)^2}} \quad (31)$$

It is clearly visible in Fig. 6 that due to the frequency shift of the black body spectrum, the first three frequency groups have gained energy while the remaining groups have lost energy. The discrepancy between the analytical and numerical solution (both averaged within frequency groups) is of the order of one percent throughout. We have also performed the test with 10 and 40 groups which did not change the errors significantly.

3.4. Velocity gradient with frequency dependent opacities

In this test, we are interested in studying the ability of the code to handle frequency-variable opacities and Doppler shifts in a flow with strong velocity gradients. The size of the box is 1.0 cm for 100 cells and is initially filled with a gas at $T = 3$ K in equilibrium with radiation and a velocity $u = \mathcal{D}x$. As a first step, we set $\mathcal{D} = 0$. In this test, the hydrodynamics are frozen and the gas density is set to $\rho = 1/(\mathcal{C}x)$ g cm⁻³ where $\mathcal{C} = 10^7$ (see below). The gas opacity varies with frequency: $\kappa(\nu) = 100$ cm² g⁻¹ for $\nu < 2 \times 10^{13}$ s⁻¹ and $\kappa(\nu) = 1$ cm² g⁻¹ for $\nu > 2 \times 10^{13}$ s⁻¹, with a smooth transition between the two regimes of width $\Delta\nu = 4.5 \times 10^9$ s⁻¹ (see Fig. 7). We use 20 frequency groups to sample the opacities. We then inject from the left hand side a radiation with a Gaussian intensity profile with a FWHM measuring 2/3 of the width of the opacities transition region which comprised the same energy as a 1000 K black body radiation.

The radiative temperatures inside the separate groups are shown in Fig. 8 (top), where only the relevant groups are presented. The radiation in the first 11 groups is rapidly absorbed by the gas which has a high opacity at these frequencies, while in the higher frequency groups, the radiation propagates rapidly in a quasi-transparent medium. The presence of radiative energy in groups 13 and above shows that the gas has been heated by the incoming radiation and has re-radiated some of its energy. Since the heated gas radiates as a black body, the radiation fills all the groups which are very narrow

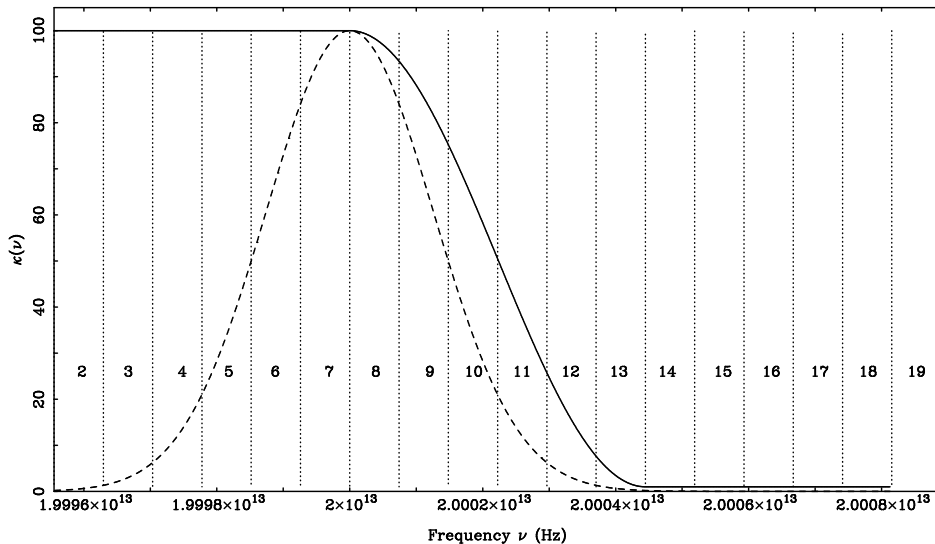


Figure 7: Gas opacity as a function of frequency in $\text{cm}^2 \text{g}^{-1}$ (solid line). Intensity of the injected radiation (normalised; dashed). The FWHM of the Gaussian radiative intensity profile measures 2/3 of the width of the opacities transition region. The vertical black dotted lines represent the frequency groups identified by their numbers.

compared to the width of a Planck curve at $T = 1000$ K. As the opacity is weak in the high groups, the radiation there can propagate freely towards the right edge of the box. The lower groups 1 to 3 are also filled by the black body radiation but their radiation cannot escape due to the strong opacities.

In order to study the effects of velocity gradients on the radiation transport, we ran a simulation with the velocity gradient $\mathcal{D} = 10^7 \text{ s}^{-1}$. In this case, $\mathcal{D} = \mathcal{C}$ and a permanent regime is achieved. The hydrodynamics are still frozen, which is justified by the fact that even the fastest gas would only have time to move a very small distance ($5 \times 10^{-5} \text{ cm}$) compared to the box size (1 cm) over the simulation time of $5 \times 10^{-12} \text{ s}$. The results are shown in Fig. 8 (bottom). We note that this time, only the radiation in the first 8 groups is absorbed and the radiation in groups 9 and above propagates freely. This shows that the radiation in the intermediate groups 9, 10 and 11 (covering the opacities transition region) was initially slightly absorbed. Then, as the Doppler frequency shift increases (due to the increasing velocity), the radiation moves to groups of higher frequencies where the opacity is much lower and the radiation is thus able to escape freely.

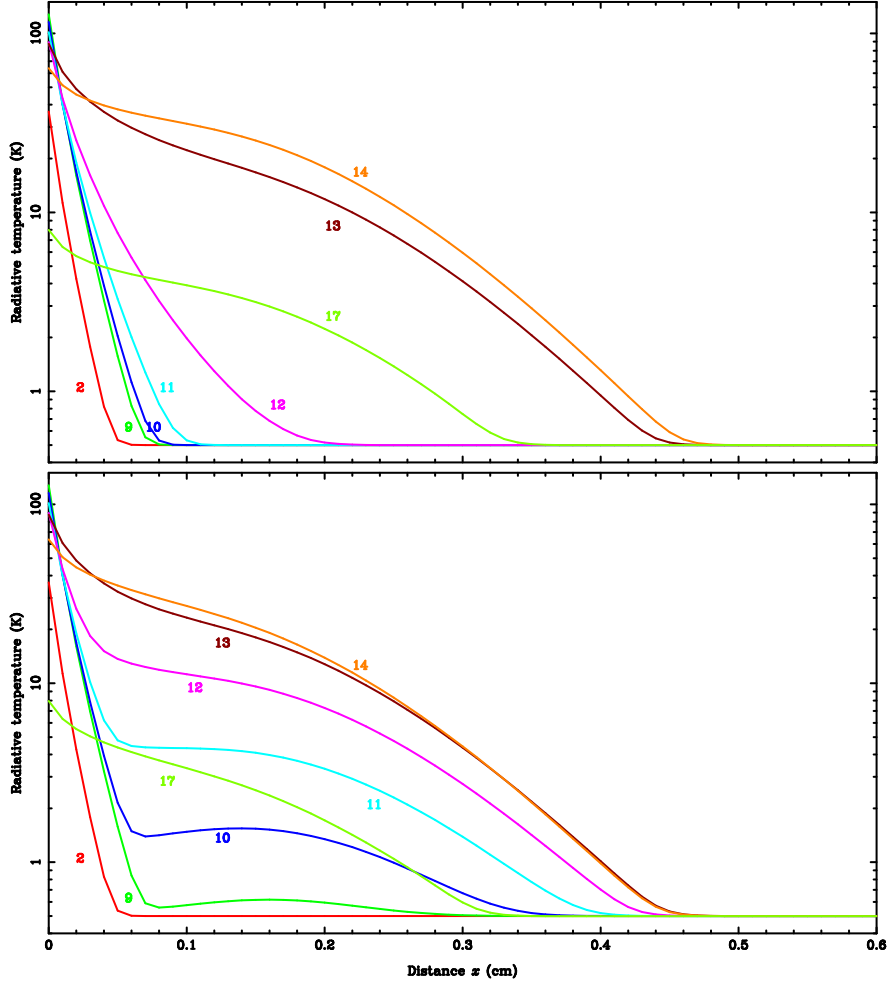


Figure 8: Group radiative temperature at time $t = 4.8 \times 10^{-12}$ s in the gradient test for a null velocity (top) and for a gas velocity which increases linearly with distance (bottom).

3.5. Astrophysical radiative shock

The next test is to make sure that the multigroup radiative transfer model is correctly coupled to the gas hydrodynamics. We ran a ‘grey’ radiative shock simulation using exactly the same parameters as in González et al. [7]. The gas inside the computational domain is initially at rest with a uniform density of $\rho = 7.78 \times 10^{-10}$ g cm $^{-3}$, temperature $T = 10$ K in equilibrium with the radiation and opacity $\kappa = 0.39$ cm 2 g $^{-1}$. The size of the box is 1.0×10^{11} cm. We give the gas at the left boundary a velocity of 20 km s $^{-1}$,

which generates the propagation of a radiative shock travelling towards the right. We use 500 equally spaced spatial zones and 6 frequency groups (5 groups evenly spaced between $\nu = 0 - 7 \times 10^{14} \text{ s}^{-1}$ and the last group holds frequencies from $7 \times 10^{14} \text{ s}^{-1}$ to ∞). The results at three different epochs are shown in Fig. 9 (solid lines). We have also run the radiative shock test with `SINERGHY1D` using only a single group and the results are shown in Fig. 9 (dashed lines). The temperature profiles are virtually indistinguishable, as illustrated by the difference ΔT between the grey and multigroup curves which is plotted below. The largest ΔT is $\sim 40 \text{ K}$ for a peak temperature of 4000 K , i.e. only one percent. Some small differences are visible in the radiative precursor. This shows that the multigroup scheme is consistent with the grey model.

We also note that the curves are identical to the ones in González et al. [7], which shows that the implicit code correctly solves the equations of RHD.

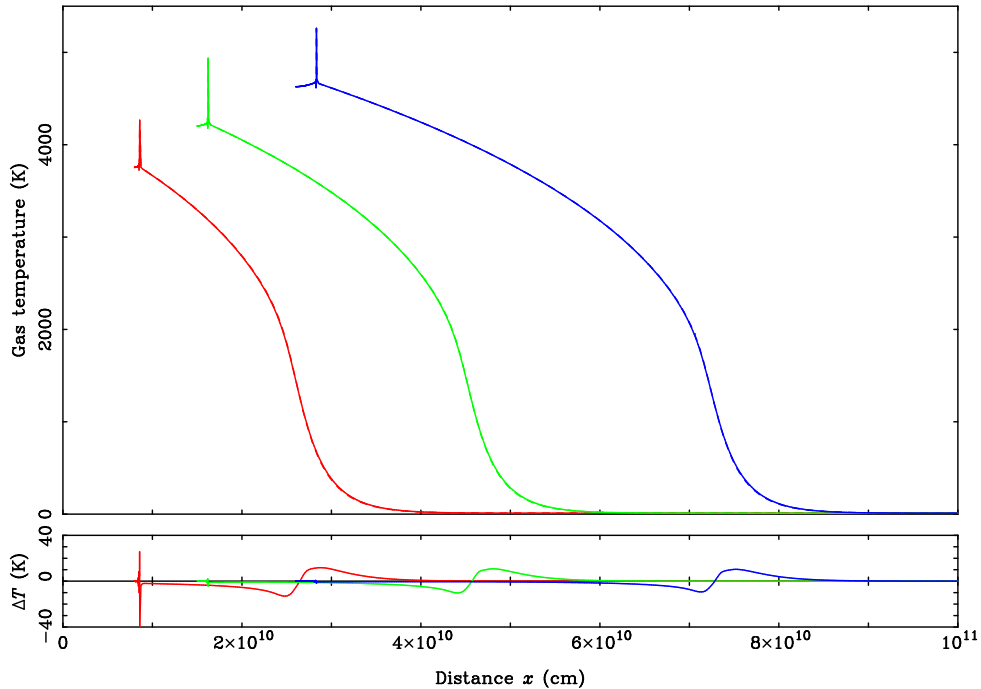


Figure 9: Gas temperature in the radiative shock test as a function of distance at times $t = 4.0 \times 10^3 \text{ s}$ (red), $7.5 \times 10^3 \text{ s}$ (green) and $1.3 \times 10^4 \text{ s}$ (blue) for the monogroup run (dashed) and the multigroup model using 6 groups (solid). The difference between the mono- and multigroup curves is shown in the bottom panel.

3.6. Multigroup radiative shock in xenon gas

Our final test is to link SINERGHY1D to the ODALISC¹ database of gas opacities in order to realistically model the evolution of a radiative shock in a xenon $^{131}_{54}\text{Xe}$ gas. The ODALISC database aims to provide spectral opacities as well as mean opacities (Rosseland and Planck) of many elements for a wide range of physical conditions.

The gas inside the box is initially at rest with a uniform density of $\rho = 10^{-3} \text{ g cm}^{-3}$, temperature $T = 1 \text{ eV}$ in equilibrium with the radiation. The size of the box is 36 cm with 550 zones; the first 100 cells have logarithmically increasing sizes, the first 500 zones cover the range 0 – 2 cm and the last 50 have steadily increasing sizes, covering the range 2 – 36 cm. We give the gas at the left boundary a velocity of 60 km s^{-1} , which generates a radiative shock travelling towards the right. We use an ideal gas equation of state with atomic mass number 131.

The opacities for the Xe gas were taken from the ODALISC database (GOMME average atom model). They depend on the gas temperature and density (often more strongly on temperature) as well as on the frequency. The opacity $\kappa(\nu)$ for the Xe gas for a density $\rho = 10^{-3} \text{ g cm}^{-3}$ and temperature $T = 1 \text{ eV}$ is shown in Fig. 10 (black solid curve). We used five groups to sample the opacities from $\nu = 10^{-3}$ to 770 eV; the colour bands in Fig. 10 illustrate the group decomposition of the frequency domain. Frequencies below 10^{-3} eV and above 770 eV are ignored, as gas temperatures in the box remain under 30 eV (except the very narrow temperature spike). The gas at such temperatures does not radiate strongly at these frequencies. We then computed the Planck (κ_{Pg}) and Rosseland (κ_{Rg}) mean opacities in each group.

Since the gas temperature and density evolve in time, the opacities need to be calculated at each timestep in each grid cell. The method we used to compute the opacities is to read in from the database a grid of opacities for the temperature range 0.01 to 100 eV and the density range 10^{-3} to 0.3 g cm^{-3} at the start of the run. From this, we then compute κ_{Pg} and κ_{Rg} in each group at each point (ρ, T) which are stored into an array. During the simulation, a particular group opacity at any T and ρ is then found using a simple four-point interpolation using the array data.

The gas and radiative temperatures for our simulation of a multigroup

¹<http://irfu.cea.fr/Projets/Odalisc/>

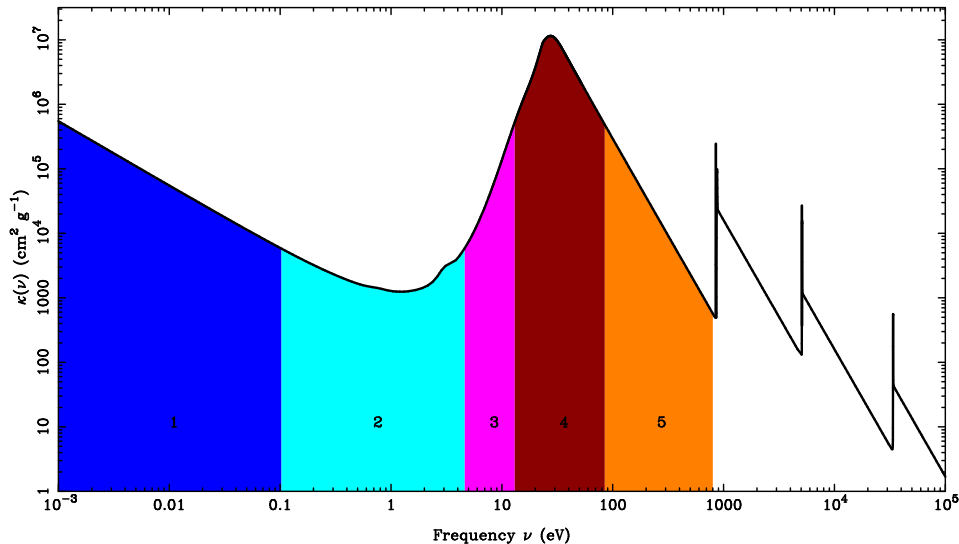


Figure 10: Xenon opacities at $\rho = 10^{-3} \text{ g cm}^{-3}$ and $T = 1 \text{ eV}$ as a function of frequencies. The colours illustrate the decomposition of the frequency domain into five groups from $\nu = 10^{-3}$ to 770 eV.

radiative shock in a Xe gas at a time $t = 10^{-9} \text{ s}$ are shown in Fig. 11 (top panel), along with the temperatures from an identical but grey run where only a single group over the same frequency range is used. A characteristic peak in the gas temperature (bright red) can be seen just around $x = 6 \times 10^{-3} \text{ cm}$ at the shock. There is a strong radiative precursor (bright green) which extends all the way to $x = 2 \text{ cm}$. The contributions to the precursor are clearly visible; at first the energy from group 5 contributes the most but subsequently gets dominated by group 4, 3 then 2 as we move further away from the shock. The radiation in the low-frequency group 1 does not appear to contribute to the dynamics of the shock. We note that the radiation in all the groups apart from group 2 gets absorbed fairly rapidly (none get past $x = 0.6 \text{ cm}$), whereas since the opacities in group 2 are the lowest (see Fig. 10), the radiation there propagates to a greater distance. Differences in the positions of the tip of the radiative precursors in the other groups further illustrate the effect of variable gas opacities.

Let us note major differences between the mutigroup and the grey models. Due to the fact that opacities are averaged over the entire frequency range (the low opacities are biased towards a higher value and vice versa), the radiation in the grey run suffers greater absorption far away from the

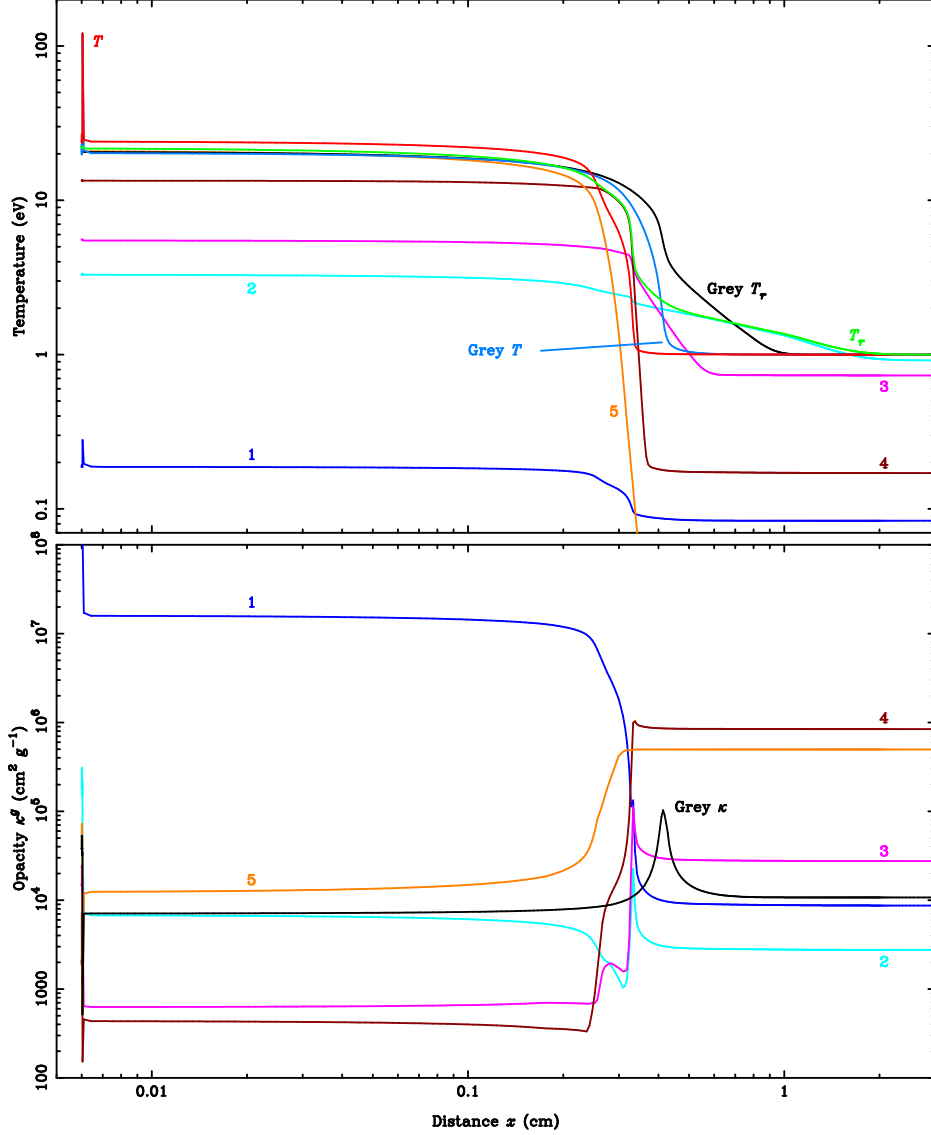


Figure 11: Top panel: Gas temperature T (bright red), total radiative temperature T_r (summed over all groups, bright green) and individual group radiative temperatures (labelled 1 to 5) in the multigroup simulation of a radiative shock in Xe gas at a time $t = 10^{-9}$ s. We have also included the gas temperature (light blue) and radiative temperature (black) from the grey run. Bottom panel: Gas opacities for each group as a function of distance. The black curve represents the opacity in the grey run (averaged over all frequencies).

shock and its radiative precursor (black curve) does not extend as far as in the multigroup case. However, between 0.3 and 0.7 cm, the grey radiative temperature is much higher than the multigroup one. For this reason, the gas is heated to a greater extent and the grey gas temperature (light blue) is higher than the multigroup one around 0.3 – 0.4 cm. We also note that the multigroup gas temperature in the range $6 \times 10^{-3} - 0.2$ cm is higher than for the grey run.

The opacities of the gas in each group and the opacity for the grey run are plotted as a function of distance in Fig. 11 (bottom panel). This is an excellent illustration of how the opacities are affected by the gas temperature. For instance, we see that the opacity in the first group is of the order of $10^4 \text{ cm}^2 \text{ g}^{-1}$ in the cold gas ahead of the radiative precursor (right hand side) whereas it gains over three orders of magnitude in the hot post-shock gas. For groups 3, 4 and 5, the opposite occurs; the opacity is high before the shock and low after. The opacities in the temperature transition region has diverse behaviours. Most importantly, the curves are very different from the grey opacity (black curve) which is very constant with a single peak around 0.4 cm corresponding to the jump in gas temperature (see light blue curve in the top panel). Interestingly, the pre- and post-shock grey opacities are very similar. It becomes very clear that the grey model cannot correctly represent the varied spectrum of opacities in such a situation, which are crucial to the evolution and dynamics of the shock.

4. Conclusions

We have developed a multigroup model for RHD using the M_1 moment model. The equations of radiative transfer are solved in the comoving frame. In order to account for the opacity variations as a function of frequency, we introduced frequency groups and applied the M_1 closure inside each of them. This gave rise to new terms depending on the frequency when coupled to the hydrodynamics. We use a finite volume method in the frequency domain in order to evaluate these new coupling terms which account for energy exchange between neighbouring groups due to the Doppler effect when strong velocity gradients are present in the gas flow.

We have verified our method using a series of tests for both radiative transfer alone and radiative transfer coupled to hydrodynamics. In the case of the radiative transfer tests, the method was found to be successful in reproducing the results obtained with a kinetic code, at a much lower com-

putational cost. We have shown that the model reverts to a grey model for frequency independent opacities and that the model is capable of treating the effects of strong velocity gradients in a gas with frequency dependent opacities.

Finally, we have coupled the SINERGHY1D code to the opacities from the ODALISC database to realistically simulate the propagation of a radiative shock in a Xe gas. We noted major differences between the multigroup and the grey models, showing the importance of accounting for the frequency variability of the gas opacities. The next step in this study will be to use a realistic equation of state for the Xe gas using the ODALISC database for more realistic simulations. ODALISC also has a number of different methods to calculate the opacities for each element. We will study the influence of the uncertainties of the opacities on the results of simulations of radiative shock in Xe in a following paper. In this work will also be included an investigation of the impact of the choice of frequency group boundaries and the number of groups on the results.

We have now begun the implementation of this multigroup method for radiative transfer in the 3D radiation magnetohydrodynamics code HERACLES [7]. The development of such a tool for hydrodynamical simulations will prove extremely important for future studies, in particular, in the field of astrophysics where high-energy radiation from bright stars or supernovae gets absorbed by dense clouds which re-radiate the energy in the infrared, or inside dense stellar atmospheres where many chemical elements are present.

Acknowledgements

The authors greatly acknowledge support from grant ANR-06-CIS6-009-01 for the programme SiNeRGHy. They would also like to thank Vladimir Tikhonchuk and Matthias González for useful comments during the writing of this paper. We also thank the referees for their valuable comments which have helped us improve this paper.

References

- [1] Blinnikov S., Lundqvist P., Bartunov O., Nomoto K., Iwamoto K., 2000, *ApJ*, 532, 1132
- [2] Buchler J. R., 1979, *JQSRT*, 22, 293

- [3] Berthon C., Charrier P., Dubroca B., 2007, *J. Sci. Comp.*, 31, 347
- [4] Charrier P., Dubroca B., Mieussens L., Turpault R., 2003, *IMA Vol. for Math. and its App.*, 135, 85
- [5] Dubroca B., Feugeas J.-L., 1999, *C. R. Acad. Sci. Paris*, 329, 915
- [6] Dubroca B., Klar A., 2002, *JCP*, 180, 584
- [7] González M., Audit E., Huynh P., 2007, *A&A*, 464, 429
- [8] Larsen E. W., Keller J. B., 1974, *J. Math. Phys.*, 15, 75
- [9] Larsen E. W., Thömmes G., Klar A., 2003, *SIAM J. Appl. Math.*, 64, 565
- [10] Larsen E. W., Thömmes G., Klar A., Seaid M., Götz T., 2002, *J. Comp. Phys.*, 183, 652
- [11] Levermore C. D., 1984, *JQSRT*, 31, 149
- [12] Levermore C. D., Pomraning G. C., 1981, *ApJ*, 248, 321
- [13] Lowrie R. B., Mihalas D., Morel J. E., 2001, *JQSRT*, 69, 291
- [14] Mihalas D., Auer L. H., 2001, *JQSRT*, 71, 61
- [15] Mihalas D., Mihalas B. D., 1984, *Foundations of Radiation Hydrodynamics*, Oxford University Press
- [16] Minerbo G. N., 1978, *JQSRT*, 20, 541
- [17] Müller I., Ruggeri T., 1998, *Rational Extended Thermodynamics*, Springer, New York
- [18] Olson G. L., Auer L. H. Hall M. L., 1998, *JQSRT*, 64, 619
- [19] Ramis R., Schmalz R., Meyer-Ter-Vehn J., 1988, *Comp. Phys. Comm.*, 49, 475
- [20] Skartlien R., 2000, *ApJ*, 536, 465
- [21] Struchtrup H., 1998, *Ann. Phys.* 266, 1
- [22] Turpault R., 2005, *JQSRT*, 94, 357